



PCCP

**Symmetry controlled photo-selection and charge separation
in butadiyne-bridged donor-bridge-acceptor compounds**

Journal:	<i>Physical Chemistry Chemical Physics</i>
Manuscript ID	CP-ART-03-2020-001235.R1
Article Type:	Paper
Date Submitted by the Author:	17-Apr-2020
Complete List of Authors:	Li, Xiao; Tulane University Valdiviezo Mora, Jesús del Carmen; Duke University, Chemistry Banziger, Susannah; Purdue University Zhang, Peng; Duke University, Chemistry Ren, Tong; Purdue University, Beratan, David; Duke University, Department of Chemistry Rubtsov, Igor; Tulane University, Chemistry

SCHOLARONE™
Manuscripts

Symmetry controlled photo-selection and charge separation in butadiyne-bridged donor-bridge-acceptor compounds

Xiao Li,^{a&} Jesús Valdiviezo,^{b&} Susannah D. Banziger,^e Peng Zhang,^b Tong Ren,^{e*} David N. Beratan,^{b,c,d*} and Igor V. Rubtsov^{a*}

^a Department of Chemistry, Tulane University, New Orleans, LA 70118, USA

^b Department of Chemistry, Duke University, Durham, North Carolina 27708, USA

^c Department of Physics, Duke University, Durham, North Carolina 27708, USA

^d Department of Biochemistry, Duke University, Durham, North Carolina 27710, USA

^e Department of Chemistry, Purdue University, West Lafayette, Indiana 47907, USA

& the authors contributed equally

Abstract

Electron transfer (ET) in donor-bridge-acceptor (DBA) compounds depends strongly on the structural and electronic properties of the bridge. Among the bridges that support donor - acceptor conjugation, alkyne bridges have attractive and unique properties: they are compact, possess linear structure permitting access to high symmetry DBA structures, and allow torsional motion of D and A, especially for longer bridges. We report conformation dependent electron transfer dynamics in a set of novel DBA compounds featuring butadiyne (C₄) bridge, N-isopropyl-1,8-naphthalimide (NAP) acceptors, and donors that span a range of reduction potentials (trimethyl silane (Si-C₄-NAP), phenyl (Ph-C₄-NAP), and dimethyl aniline (D-C₄-NAP)). Transient mid-IR absorption spectra of the C≡C bridge stretching modes, transient spectra in the visible range and TD-DFT calculations were used to decipher the ET mechanisms. We found that the electronic excited state energies and, especially, the transition dipoles ($S_0 \rightarrow S_n$) depend strongly on the dihedral angle (θ) between D and A and the frontier orbital symmetry, offering an opportunity to photo-select particular excited states with specific ranges of dihedral angles by exciting at chosen wavelengths. For example, excitation of D-C₄-NAP at 400 nm predominantly prepares an S_1 excited state in the planar conformations ($\theta \sim 0$) but selects an S_2 state with $\theta \sim 90^\circ$, indicating the dominant role of the molecular symmetry in the photophysics. Moreover, the symmetry of the frontier orbitals of such DBA compounds not only defines the photo-selection outcome, but also determines the rate of the $S_2 \rightarrow S_1$ charge separation reaction. Unprecedented variation of the S_2 - S_1 electronic coupling with θ by over four orders of magnitude results in slow ET at θ ca. 0° and 90° but extremely fast ET at θ of 20 - 60° . The unique features of high-symmetry alkyne bridged DBA structures enable frequency dependent ET rate selection and make this family of compounds promising targets for the vibrational excitation control of ET kinetics.

1. Introduction

* To whom correspondence should be addressed. E-mail: tren@purdue.edu; david.beratan@duke.edu; irubtsov@tulane.edu

Compounds featuring conjugated bridging motifs attract strong interest because these bridges enable significant coupling of the localized electronic states. Compounds of this kind enjoy applications as light harvesting chromophores,¹⁻³ nonlinear absorbers and optical limiters,⁴⁻⁶ as well as generators of application for photoinduced charge separation (CS).^{7, 8}

A range of conjugated bridge structures appears in donor-bridge-acceptor (DBA) compounds, including alkenes,⁹⁻¹⁴ phenylenes,¹⁵⁻¹⁷ stilbenes,¹⁸ and alkynes,¹⁹⁻²⁴ as well as motifs with more extended or mixed π structures.²⁵⁻³¹ Alkyne bridges are particularly attractive as they offer compact, linear structures that supports conjugation. While rather rigid with respect to bending, alkyne bridges feature small barriers to torsional rotation of the D and A moieties, producing a wide distribution of dihedral angles in the ground state (GS).³²

Compounds with butadiyne bridges that link weakly reducing donor and weakly oxidizing acceptor moieties were developed as chromophores and broad-band white-light fluorophores.³³ The large emission frequency width in these compounds originates from contributions of locally excited and partially charge-separated states.³³⁻³⁵ The high emission quantum yields in these systems suggests that their extent of charge separation is low.

Here, we explored the excited state and electron transfer properties of compounds where D and A are linked by a butadiyne (C4) bridge. A strong electron acceptor (NAP) was used with donors of various oxidation potentials, including a rather strongly reducing electron donor. Compounds of this kind have the potential to serve as “smart” chromophores responding to the environment, where photoinduced electron transfer (ET) rates may be modulated by external stimuli.

The torsion angle distribution in butadiyne bridged compounds is expected to depend on the nature of the bridging moieties. The Albinsson and Anderson groups measured and computed the rotation free energy barriers in butadiyne bridged metal porphyrins,^{32, 36} finding the rotational barriers to be less than $k_B T$ and that the planar conformations are favored. They also found that porphyrin-to-porphyrin coupling produces excited states that are fully delocalized on the porphyrins in the planar geometries, while orthogonal conformations of the porphyrins are electronically decoupled.^{37, 38} The noted sensitivity of the electronic coupling to the torsion angle influences the absorption spectra, allowing selective excitation of either planar or orthogonal conformation in the Q or Soret band of the porphyrin (P).^{37, 38} Planarization in P-C4-P chromophores was achieved by axial ligation with a specially designed ligand that chelates both porphyrins. This butadiyne linked porphyrin dimer was also used as a bridge linking a ferrocene donor with a C_{60} acceptor.³⁷ Both CS and charge recombination (CR) rates were found to be significantly slower in the structures with orthogonal porphyrins.³⁷

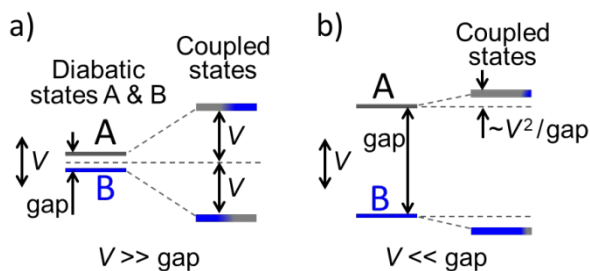
A large number of studies has examined the dihedral angle dependence of the electronic couplings in poly-phenylene bridged DBA structures.³⁹⁻⁴³ For example, studies of Harriman and coworkers⁴⁴ used an elegant tethered strap approach to study how the torsion angle between two phenyl moieties in C_2 -Ph-Ph- C_2 bridges influences electronic couplings. Connecting a $Ru^{II}(tpy)_2$ / $Os^{II}(tpy)_2$

donor-acceptor pair with this bridge, they found a dramatic decrease in the electronic coupling for the species with a 90° torsion angle between the two phenyl rings.⁴⁴

The ET rate between a donor and acceptor is influenced by the electronic coupling (in the non-adiabatic or weak coupling regime), the reorganization energy, and the reaction free energy.⁴⁵ The bridge electronic structure and DA separation distance determine the electronic coupling.⁴⁶⁻⁴⁸ The torsion angle between the D and A has a particularly strong influence on the bridge-mediated DA coupling, and extensive theoretical and experimental studies have characterized the bridge-mediated coupling.^{38, 49-51}

A particularly useful feature of the alkyne bridges is that they can support DBA conformations with a symmetry plane (C_S) for the D and A moieties being either coplanar and orthogonal. As a result, the interactions among the D and A localized frontier orbitals may be tuned, and the nature of the optical excitation, charge separation, and recombination can be controlled. Here, we demonstrate a unique feature of the alkyne bridged DBA compounds where symmetry defines the excited state and ET properties, making this class of DBA species attractive targets for ET rate modulation through conformational control via external stimuli.⁵²⁻⁵⁵

Alkyne bridges are capable of supporting strong bridge-mediated coupling of D and A electronic states. If the CS state in these species is coupled strongly to a D- or A-localized state, the coupling produces eigenstates, that are an equal mixture of the two diabatic state wavefunctions.⁵⁶ This mixing can reduce dramatically the CS character of the two eigenstates, limiting it to only 50% (Scheme 1a). To increase the CS state character with a fixed coupling strength, the energy gap between the diabatic CS and D- or A-localized state(s) has to be increased to become larger than the coupling energy, thus eliminating the strong coupling condition (Scheme 1b). This can be achieved, for example, by using a more strongly reducing electron donor, thus lowering the diabatic CS state energy (Scheme 1b), or by selecting a more polar solvent which will stabilize the radical cation / radical anion charge separated state. The dihedral angle between D and A, θ , is a key determinant of the electron coupling strength and the non-adiabatic ET rate.



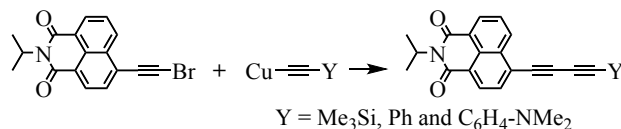
Scheme 1. Coupled states for strong (a) and weak (b) coupling regimes, defined by the relation between the diabatic state (A, B) interaction energy, V , and their energy gap.⁵⁷

The novel butadiyne (C4) bridged DBA structures studied here have an *N*-isopropyl-1,8-naphthalimide (NAP) acceptor and various donors (Fig. 1). Femtosecond-nanosecond transient absorption measurements in the visible and mid-IR regions following 400 nm excitation were performed for Si-C4-

NAP, Ph-C4-NAP and D-C4-NAP in dichloromethane (DCM) and toluene solvents. Transient mid-IR spectra of the C≡C bridge stretching modes were found to be critical for understanding the excited state electronic dynamics. Formation of a highly polarized state, namely the charge separated state (CSS), was observed in D-C4-NAP. Vibronic relaxation, charge separation, dihedral angle (θ) equilibration, charge recombination, and triplet state formation were tracked in the excited electronic states. TD-DFT analysis of the excited electronic states and normal mode analysis enabled the assignment of the observed dynamics to specific electronic transitions. We have shown that the torsional barrier to rotation in the ground state is less than $k_B T$, providing access to a wide range of dihedral D-A angles. Excited state dynamics, including CS, is strongly influenced by the dihedral angle. The observations are rationalized, as well, based on frontier orbital symmetry. Interestingly, the torsional motion, and the associated spectroscopic changes, allows interrogation of the ET dynamics associated with molecular sub-populations.

2. Experimental Details

Synthesis. All three DBA compounds featuring the butadiyn-diyl bridge moiety (referred to as a butadiyne bridge) were prepared using the Cadiot-Chodkiewicz coupling reactions⁵⁸ between 4-bromoethynyl-N-isopropyl-1,8-naphthalimide ($\text{BrC}_2\text{NAP}^{\text{IPr}}$) and an appropriately substituted ethyne (Scheme 2). These compounds were characterized by UV-Vis, FTIR and ^1H NMR spectroscopic techniques. The details of synthesis and characterization are provided in the Supplementary Materials.



Scheme 2. Synthesis of DBA compounds featuring butadiyne bridge.

Time-resolved and linear measurements in the visible and mid-IR regions. Transient UV/Vis pump – Vis/m-IR probe measurements were performed using an in-house built spectrometer.^{59, 60} A Ti:Sapphire fs oscillator (Vitesse, Coherent Inc.) and regenerative amplifier (Spitfire, Spectra Physics) produced pulses at 804 nm, with 44 fs duration at 1 kHz repetition rate. A portion of the beam was frequency doubled and 402 nm pulses, of 1–1.5 $\mu\text{J}/\text{pulse}$, were used to electronically excited the compounds. Another portion of the 804 nm beam was used to pump an optical parametric amplifier and to generate mid-IR pulses tunable from 1000 to 4000 cm^{-1} with pulse energies of ca. 1 μJ and spectral width of ca. 200 cm^{-1} . The mid-IR pulses were used to produce vibrationally excited species. The third portion of the 804 nm beam (ca. 7 $\mu\text{J}/\text{pulse}$) was used for white light continuum (WLC) generation in a sapphire wafer; the WLC served as a probe beam in the visible and near-IR regions. All three beams overlapped in the sample, but either a visible/near-IR or mid-IR probe beam was used in the experiments. Transient spectra in the visible region were measured with a CCD camera (PIXIS-100, Princeton Instrument) mounted to a monochromator (TRIAX-190, Horiba); the mid-IR spectra were measured with a single-channel MCT

detector (Infrared Associates). Time resolved and linear measurements were performed in a flow cell with 2 mm CaF₂ windows and of 100 μm optical pathlength at room temperature (22 ± 0.5 °C).

Computational details. DFT and TD-DFT calculations for Si-C4-NAP, Ph-C4-NAP and D-C4-NAP were performed using the MN15 functional⁶¹ and the Def2-SVP basis set⁶² as implemented in Gaussian 16.⁶³ The MN15 functional was chosen based on its close agreement with the experimental vibrational frequencies and electronic spectra. The CAM-B3LYP functional⁶⁴ was also tested and showed similar results. The polarizable continuum model (PCM)⁶⁵ was used to simulate the solvent effects of toluene and dichloromethane in the DFT and TD-DFT analysis. Torsion angles of 0, 15, 30, 60, 75, and 90° between D and A moieties were fixed to evaluate the influence of torsion angle on the vibrational spectra and electronic couplings. For cases where torsional conformations do not correspond to energy minima, projected frequencies were calculated.⁶⁶

Electronic couplings between the S₁ and S₂ states (H_{ab}) were calculated using the generalized Mulliken-Hush (GMH) method⁶⁷ (Eq. 1).

$$H_{ab} = \frac{\mu_{12}\Delta E_{12}}{\sqrt{(\mu_1 - \mu_2)^2 + 4\mu_{12}^2}} \quad (1)$$

Here, μ_{12} is the transition dipole moment between the S₁ and S₂ state, ΔE_{12} is the energy difference between the S₁ and S₂ states, μ_1 is the S₁ dipole moment, and μ_2 is the S₂ dipole moment. The transition dipole moments between excited states were computed in Dalton 2018⁶⁸ using quadratic response theory with the CAM-B3LYP functional, and the same basis set was used as in the TD-DFT analysis. Dipole moments and energy differences were obtained from TD-DFT calculations with the MN15 functional.

3. Results and Discussion

3.1. Steady-state absorption and emission spectra

The absorption and normalized emission spectra of the three compounds studied are shown in Figure 2. A clear mirror image of the emission spectra with preserved vibrational structure is found for the Si-C4-NAP and Ph-C4-NAP emission and absorption spectra in both toluene and DCM solutions. The Stokes shift is small (~1000 cm⁻¹) and essentially solvent independent for Si-C4-NAP (Fig. 2a), indicating that both the ground and relaxed excited states are only weakly polarized. For Ph-C4-NAP, the absorption spectrum changes weakly with solvent polarity, indicating small polarization of the ground state. However, both the emission spectrum and the Stokes shift for Ph-C4-NAP depend strongly on the solvent polarity (Fig. 2b), indicating significant solvent reorganization to accommodate a polarized excited state. With an increase of the donor strength in D-C4-NAP (Fig. 1), a new absorption peak appears at lower frequencies, red-shifted by ca. 5000 cm⁻¹. The absorption peak width is sensitive to the solvent polarity, indicating a larger polarization of the Frank-Condon excited state, compared to that for Ph-C4-NAP. The Stokes shift for D-C4-NAP is extremely large and solvent dependent, reaching 7000 cm⁻¹ in DCM. This shift indicates very high polarization of the excited state (Fig. 2c) and suggests that the

charge-separated state is observed directly in the linear absorption and emission spectra. The DFT calculations confirm that the CSS in D-C4-NAP is indeed a bright state, deriving its oscillator strength from a higher-energy electronic state, S_3 . Interestingly, this electronic state (S_3) is similar to the lowest energy NAP-based excited state observed for Si-C4-NAP (Figures S1, S2, S9).

The fluorescence quantum yield (QY) is high among the compounds studied here when they lack a strong donor (i.e., Si-C4-NAP and Ph-C4-NAP), especially in toluene solvent (Table 1). The emission for D-C4-NAP in toluene is also high (QY~27.2%), and the spectra are significantly red shifted ($\lambda_{\text{max}} = 575$ nm). For D-C4-NAP in DCM, the emission is weak (QY~1.24%) and strongly red shifted ($\lambda_{\text{max}} = 680$ nm), indicating that the emission originates from a highly polarized state. The extent of charge separation is discussed below.

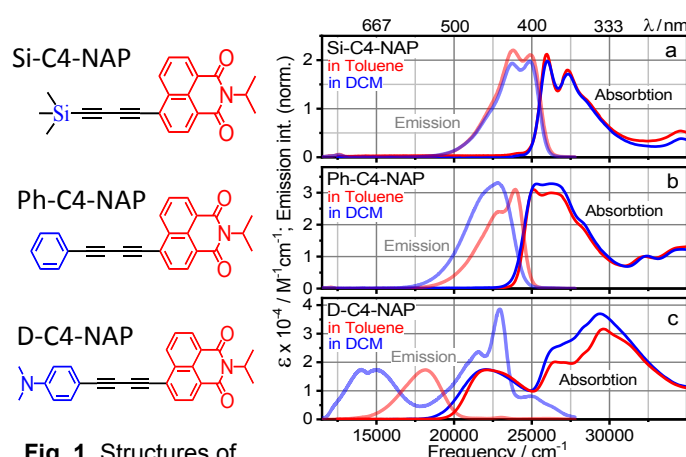


Fig. 1. Structures of the compounds used.

Fig. 2. Absorption (bright lines) and emission (light lines, $\lambda_{\text{exc}} = 340$ nm) spectra of (a) Si-C4-NAP, (b) Ph-C4-NAP, and (c) D-C4-NAP in toluene (red lines) and DCM (blue lines).

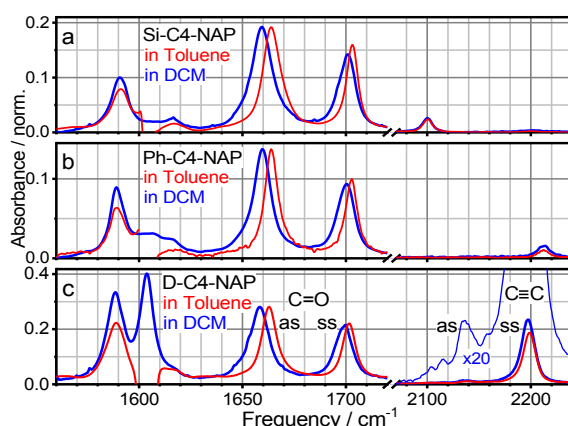


Fig. 3. Solvent subtracted FTIR absorption spectra of the three compounds amplitude normalized at the C=O as mode. Strong toluene absorption at ca. 1605 cm⁻¹ prevented accurate measurements in this region.

Table 1. Emission quantum yields for the indicated compounds in two solvents.[&]

	In toluene, %	In DCM, %
Si-C4-NAP	52.7±1.4	43.3±1.8
Ph-C4-NAP	52.1±1.8	34.2±0.4
D-C4-NAP	27.2±0.5	1.24±0.11

[&]Excitation wavelength: 340 nm.

The vibrational absorption spectra (FTIR) of the three compounds studied here feature several strong vibrational transitions (Fig. 3), including symmetric and asymmetric carbonyl stretching modes of NAP ($\nu_{\text{ss}}(\text{C}=\text{O})$, $\nu_{\text{as}}(\text{C}=\text{O})$, see labels in Fig. 3c) and two strong phenyl (donor) and naphthyl (NAP) ring deformation modes around 1600 cm⁻¹, involving CC stretching and CH in-plane bending at the two moieties. The lower frequency peak of the two (~1589 cm⁻¹) belongs mostly to NAP and is present for all three compounds. The higher frequency peak (1604 cm⁻¹) is mostly located at the donor moiety and is strong only in D-C4-NAP. Despite large distance between the phenyl and naphthyl moieties of ca. 6.7 Å, the DFT calculations revealed a partial (10-20%) mixing of the donor and acceptor vibrational modes, suggesting that their conjugation-facilitated coupling is ca. 3 cm⁻¹.

The butadiyne (C4) bridge features two strongly delocalized $\nu_{C\equiv C}$ stretching normal modes – symmetric ($\nu_{C\equiv C,ss}$) and antisymmetric ($\nu_{C\equiv C,as}$). However, a single vibrational absorption peak dominates the spectrum for each compound, typically arising from a symmetric stretching mode. For example, for D-C4-NAP, the peak at 2198 cm^{-1} arises from $\nu_{C\equiv C,ss}$, while the $\nu_{C\equiv C,as}$ peak is seen at 2136 cm^{-1} (computed at 2118 cm^{-1}) with ca. 20-fold weaker IR intensity (Fig. 3c, thin blue line, Table S1 for DFT).

For the Ph-C4-NAP species, the peak at ca. 2212 cm^{-1} arises from a symmetric stretching mode; it is much weaker than the corresponding mode for the D-C4-NAP species (Fig. 3b). A similarly weak single $\nu_{C\equiv C}$ peak is found for Si-C4-NAP at $\sim 2100 \text{ cm}^{-1}$; it arises from an antisymmetric stretching mode (Fig. 3a). The IR intensity of $\nu_{C\equiv C,ss}$ for Ph-C4-NAP and D-C4-NAP derives from light-induced polarization of the molecule across the bridge in the GS. This polarization is indicated from the shift in the $C\equiv C$ peak frequency for D-C4-NAP in the more polar DCM solvent (Fig. 3c). Transient absorption spectroscopy in the mid-IR and visible spectral regions, and DFT calculations, were employed to understand the charge distributions in these compounds and the excited state dynamics.

3.2. Transient absorption spectroscopy in the mid-IR and visible spectral regions

Figure 4 shows transient absorption spectra of the three compounds in the visible (left) and mid-IR spectral regions (middle) at selected delay times (see insets) following excitation at 400 nm. The spectral changes are measured over a time window ranging from sub-picoseconds to ca. 3.5 ns. The spectral changes in the visible range are large in all compounds. Except for D-C4-NAP in DCM, these transient features do not decay to zero at large pump - probe delay times, revealing the formation of a long-lived state and the absence of the GS recovery. This long-lived state is assigned to a NAP localized triplet state (^TNAP), based on the similarity of the transient features in all three compounds, including the Si-C4-NAP species that lacks a donor group, the long lifetime of the state that exceeds 10 ns, and the characteristic changes of the NAP C=O frequencies that both experience a ca. 50 cm^{-1} red shift compared to the GS frequencies. These observations are consistent with the DFT-computed $\nu_{C=O}$ changes for the ^TNAP state (Table S3).

The extent of the GS recovery in these compounds can be judged from the ground state bleaching (GSB) signals of the C=O stretching modes of NAP. Except for D-C4-NAP in DCM, where the GS recovery is complete within a nanosecond, only a partial GS recovery is observed for other compounds, apparent from the presence of the GSB peaks at ca. 1705 and 1665 cm^{-1} at large delay times of 1-3 ns. Therefore, the large changes in the transient visible spectra (Fig. 4a-d) in the ns time scale are associated with the formation of the ^TNAP state.

Decay-associated spectral analysis and global fitting. The transient spectral data in the visible region were fitted using a decay-associated spectral (DAS) approach; an example of the DAS analysis is shown in Figure 5 for D-C4-NAP in DCM. Three principle time components are required to describe the spectral dynamics. The fastest component (0.63 ps) produces a strong increase of the excited state absorption (ESA) across the spectrum, peaking at 590 nm (red line). This feature is assigned to relaxation of the

excess energy, *vide infra*. The second component of 4.3 ps is associated with the absorbance decay at 525 nm and rise at 475 nm. We assign this feature to a transition between the excited electronic states based on the changes in the mid-IR spectrum. The slow decay component of 0.26 ns describes the GS recovery.

Simultaneous fittings of the characteristic kinetics in the visible and mid-IR regions were performed for each compound (Fig. 4, right). The characteristic times found in these fits differ slightly from the global fits involving either the Vis or mid-IR data, suggesting that the processes that occur are complex (not necessarily single exponential) and contribute differently in the visible and in their mid-IR regimes. For example, the process occurring with ca. 50 ps time constant for D-C4-NAP in DCM, apparent in the mid-IR spectra, is not seen clearly in the global fit of the visible transient spectral data. However, the observed variations, e.g. 4.3 ps vs. 5.5 ps for the second fastest time component for D-C4-NAP in DCM, are not considered to be essential, indicating larger actual error bars for the presented time components. The global fit involving characteristic kinetics across the Vis and mid-IR transient spectra is considered to be the most representative of the dynamics, as discussed below.

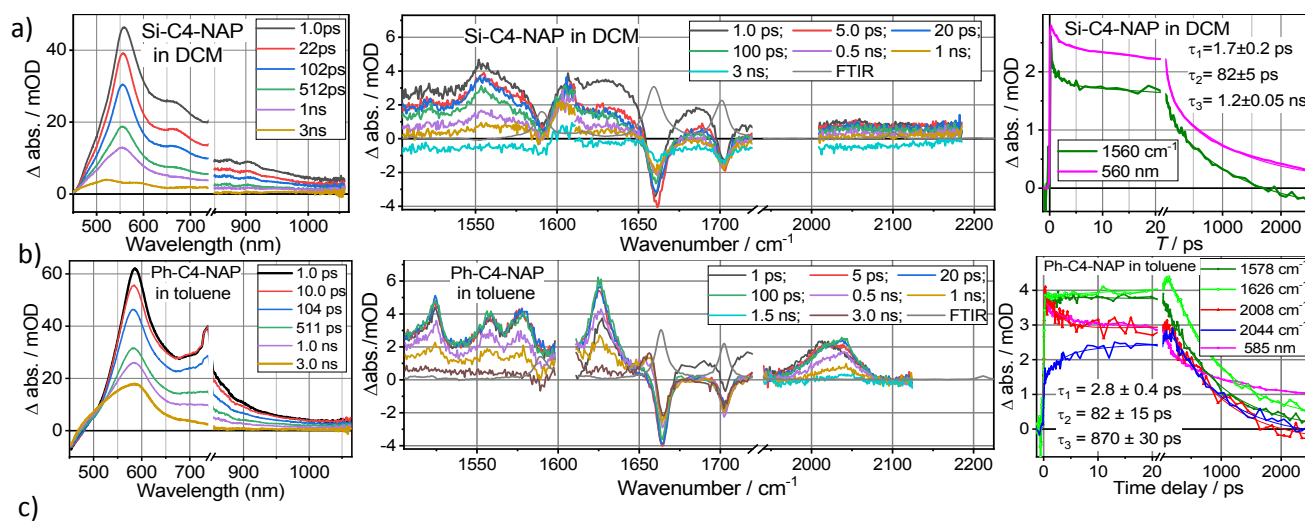
Spectral dynamics for Si-C4-NAP and Ph-C4-NAP. For the Si-C4-NAP species in DCM (Fig. 4a) and toluene (Fig. S3), the kinetics measured in the visible and fingerprint regions have essentially the same time evolution (Fig. 4a, right); nevertheless, their fitting requires a three-exponential function. The fast 2.4 ps component in toluene and of 1.7 ps in DCM is assigned to vibrational cooling of the excess energy introduced by the 400 nm pump. The slow decay component of 1.6 ns in toluene and 1.2 ns in DCM is associated with intersystem crossing (k_{ISC}) and formation of ^1NAP ; the middle decay component of ca. 80 ps is discussed below. The transient absorption of the C=C bridge modes (1950-2100 cm^{-1}) is weak in the excited state, indicating weak polarization of the molecule across the bridge.

The transient spectra in the visible and fingerprint regions for Ph-C4-NAP in both solvents are similar to those measured for Si-C4-NAP (Fig. 4a-c), indicating formation of the ^1NAP state at later times. The fingerprint (FP) region shows multiple transient absorption peaks, but with a rather simple decay kinetics (see Fig. 4b, right, light green and green curves). However, in contrast to the Si-C4-NAP species, the $\nu_{\text{C}=\text{C}}$ peak for the Ph-C4-NAP species is greatly enhanced, compared to the $\nu_{\text{C}=\text{C}}$ absorption in the GS (Fig. 4b,c, grey line), indicating strong ES bridge polarization, and its frequency is red shifted by ca. 200 cm^{-1} in toluene and by ca. 170 cm^{-1} in DCM, measured at small time delays. In DCM (Fig. 4c) the $\nu_{\text{C}=\text{C}}$ ESA peak is narrow and shows no shift with time but grows slightly, whereas in toluene the initially formed peak at 2010 cm^{-1} decays while a blue-shifted peak at 2040 cm^{-1} grows; an isosbestic point at ca. 2022 cm^{-1} is apparent during the first 100 ps, suggesting involvement of just two states. The decay of the peak at 2010 cm^{-1} is partial – both peaks are apparent in the transient spectra at $T > 100$ ps, and their ratio does not change at later times, *vide infra*. A three-exponential function is required to characterize the dynamics of Ph-C4-NAP globally in each solvent, resulting in the characteristic time constants of $\tau_1 = 2.8 \pm 0.4$ ps, $\tau_2 = 82 \pm 15$ ps, and $\tau_3 = 870 \pm 30$ ps in toluene and $\tau_1 = 1.6 \pm 0.2$ ps, $\tau_2 = 80 \pm 5$ ps, and $\tau_3 =$

560 ± 30 ps in DCM. Similar to Si-C4-NAP, the characteristic times for Ph-C4-NAP are systematically shorter in DCM compared to those in toluene.

Spectral dynamics for D-C4-NAP. The dynamics for D-C4-NAP in toluene (Fig. 4d) is similar to that for Ph-C4-NAP; formation of the 1 NAP state is apparent in the visible and FP regions at later times. Note that the transient absorption spectrum in the visible region is affected by the stimulated emission at ca. 570 nm (see emission spectrum in Fig. 2c). The $\nu_{C\equiv C}$ ESA peaks show a spectacular transition dipole enhancement. At early times the $\nu_{C\equiv C}$ absorption is extremely broad with a main peak at 2080 cm^{-1} and a smaller peak at 1985 cm^{-1} . Assuming that the lower frequency $C\equiv C$ peak is found in a state with higher polarization extent across the bridge (*vide infra*), the observed shift to lower frequencies suggests an increase of the polarization extent of the ES with time.

Very different dynamics is found for D-C4-NAP in DCM compared to other compounds and to D-C4-NAP in toluene. The dynamics shows a dramatic spectral change in the visible range within the first 10 ps after excitation (Fig. 4e), involving a strong rise at ca. 580 nm and a change in spectral shape. Formation of 1 NAP at later times is not observed; instead the transient spectra decay to zero with the 0.38 ns time, exhibiting complete recovery of the GS. The transient spectra in the $C\equiv C$ region also shows strong absorbance enhancement and large red shift of the ESA peaks. The initial $C\equiv C$ ESA is found predominantly at 2090 cm^{-1} , while a second peak at ca. 2030 cm^{-1} grows with time and the peak at 2090 cm^{-1} decays slightly, suggesting the presence of two electronic states with different bridge polarization extent. Global fits to the kinetics for D-C4-NAP in both solvents requires four time components (Fig. 4d,e right panel), in contrast to the findings in the two other compounds which require just three components to fit. Despite the large number of the fitting components, the time components are well constrained as they describe characteristic spectral changes. The obtained time constants for all compounds are shown in the right panel inset of Figure 4 and in Table 2; the designated processes are shown in Figure 5.



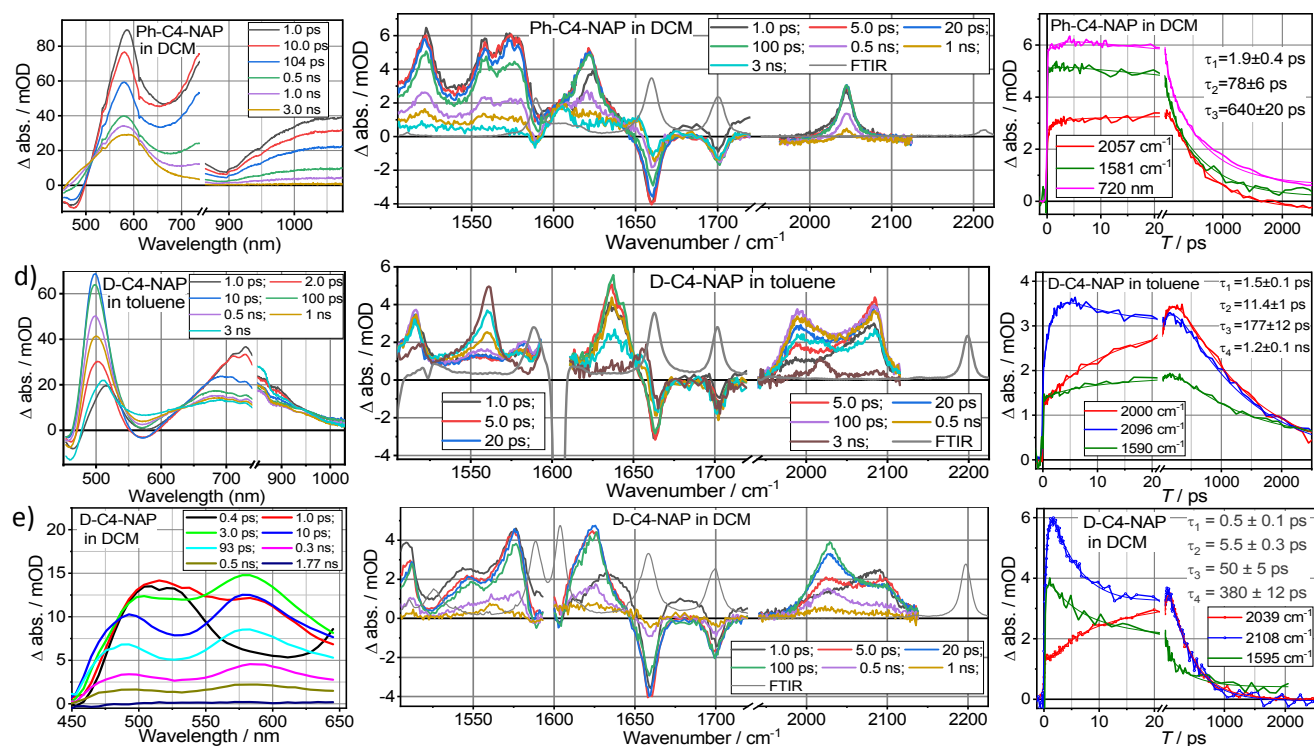


Fig. 4. Transient spectra in the visible (left panel) and mid-IR (middle panel) regions for Si-C4-NAP (a), Ph-C4-NAP (b, c), and D-C4-NAP (d, e) compounds in toluene and DCM (indicated) measured at indicated time delays following 400 nm excitation. The mid-IR transient spectra also show scaled linear absorption spectra (FTIR, grey line). Right panels show selected characteristic kinetics and the results of a global fitting with multi-exponential function (thin lines of matching colors); the resulting time constants are shown as insets.

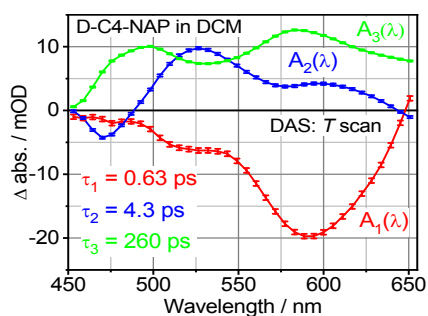


Fig. 5. Decay-associated spectra for D-C4-NAP in DCM; the obtained time constants of $\tau_1 = 0.63 \pm 0.07$ ps, $\tau_2 = 4.3 \pm 0.5$ ps, and $\tau_3 = 260 \pm 30$ ps.

Assignment of the slowest component in all three compounds. The slowest measured ns component reflects either the GS recovery (k_{CR} , D-C4-NAP in DCM) or the ^TNAP state formation (k_R , all other cases) (Fig. 5). The second slowest time component, k_{rot} , ranges from 50 to 177 ps for the three compounds. In contrast to the Si-C4-NAP species, where this component causes just a decrease of the transient absorption across the FP region, in Ph-C4-NAP and D-C4-NAP it is manifested in an increase of absorbance across the C≡C and FP absorption peaks (Fig. 4b-e). The characteristic times of 50 – 177 ps are too slow to be described by solvation⁶⁹ or vibrational cooling.^{70, 71} For the Ph-C4-NAP and D-C4-NAP

compounds, we assign this component to the dynamics associated with the changes of the DA dihedral angle distribution. Note that this component is not apparent in the visible transient spectra.

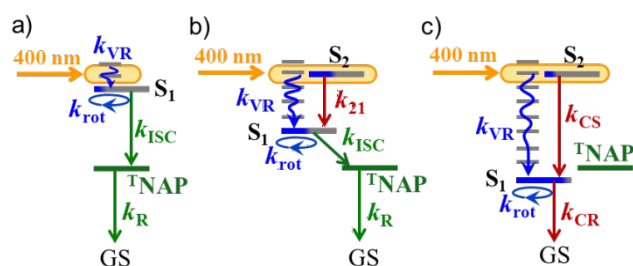


Fig. 6. Three characteristic energy diagrams involving the states relevant for transient absorption with 400 nm excitation. Diagram a) describes behavior of Si-C4-NAP in both toluene and DCM solvents involving a single singlet excited state, S₁. Diagram b) is characteristic for Ph-C4-NAP in both solvents and for D-C4-NAP in toluene, although the polarization extent for the states S₂ and S₁ varies for different systems. 400 nm radiation excites S₂ and vibrationally hot S₁ states. The triplet state is the lowest energy excited state for a) and b) panels. Diagram c) describes D-C4-NAP in DCM where the S₁ state, which is essentially the CSS, is the lowest energy state. The charge separation, $k_{CS} = (5.5 \text{ ps})^{-1}$ occurs much faster than charge recombination, $k_{CR} = (0.38 \text{ ns})^{-1}$; accumulation of the T¹NAP state is not observed. All measured rate constants are shown in Table 2.

Assignment of fast components. Each compound has one or two time components in the ps range; their origins differ for different components. For Si-C4-NAP, the fastest component (2.4 ps in toluene and 1.7 ps in DCM) is associated with vibrational cooling and solvation of the NAP-based excited state, manifested in absorbance decays in the FP and Vis regions (Fig. 4a). The fastest component for D-C4-NAP, observed at 1.5 ps in toluene and 0.5 ps in DCM (Fig. 4d,e), is manifested in a strong rise of the visible peak at ca. 600 nm and small changes of the C≡C band spectral shape. It is assigned predominantly to vibrational relaxation in the excited state manifold, but likely also has contributions derived from solvation. Note that the energy of the absorbed photon at 400 nm is ca. 5000 cm⁻¹ higher than the energy of the lowest bright transition in D-C4-NAP (Fig. 2c).

For the Ph-C4-NAP and D-C4-NAP compounds, featuring additional electronic states associated with charge transfer from the donor to acceptor, there is a component manifested in an increase of one C≡C peak and a decrease of another C≡C peak in the excited state (Fig. 4b,d,e). For example, for D-C4-NAP in toluene (Fig. 4d), the 11.4 ps component causes a decay of the blue-shifted peak at 2096 cm⁻¹ and a rise of the red-shifted peak at 2000 cm⁻¹. For Ph-C4-NAP in toluene, the C≡C peak, found at early delay times at 2010 cm⁻¹, decays and the peak at 2043 cm⁻¹ rises with the same characteristic time of 2.8 ps. Such spectral changes are assigned to the transition between excited electronic states; depending on the molecular system the dynamically formed excited state features either higher or lower polarization extent. The blue shift of the peak with time, as for Ph-C4-NAP, suggests formation of a state with a smaller contribution of the pure CCS state compared to that into the higher-energy eigenstate. Dynamics appearance of the red shifted peak for D-C4-NAP suggests formation of the state with a higher polarization extent. Note that the C≡C transient absorption peak for Ph-C4-NAP in DCM, observed initially at 2045 cm⁻¹, does not shift with time, indicating similar polarization extents of the two involved

eigenstates. Surprisingly, the modes in the FP region showed much smaller changes, compared to the changes of the C≡C peaks (*vide infra*).

Table 2. Rate constants determined for excited state dynamics for Si-C4-NAP, Ph-C4-NAP, and D-C4-NAP in toluene and DCM.

	Si-C4-NAP in toluene	Si-C4-NAP in DCM	Ph-C4-NAP in toluene	Ph-C4-NAP in DCM	D-C4-NAP in toluene	D-C4-NAP in DCM
$1/k_{VR}$, ps	2.4	1.7	--	--	1.5	0.5
$1/k_{21}$; $1/k_{CS}$, ps	--	--	2.8	1.9	11.4	5.5
$1/k_{obs}$, ps	72	82	82	78	177	50
$1/k_{CR}$, ns	--	--	--	--	--	0.38
$1/k_{ISC}$, ns	1.6	0.87	0.87	0.64	1.2	--
$1/k_R$	>10 ns	>10 ns	>10 ns	>10 ns	>10 ns	--

The observed transient spectral dynamics for Ph-C4-NAP and D-C4-NAP are consistent with the involvement of two singlet excited states featuring different polarization extents: for D-C4-NAP in both solvents the polarization extent in the S_1 state is much larger than that in the S_2 state suggesting that the S_1 state is essentially the CS state (Fig. 6b,c); the situation is reversed for Ph-C4-NAP in toluene whereas for Ph-C4-NAP in DCM the polarization extents of S_1 and S_2 are similar.

3.3. TD-DFT computation results

Torsion angle distribution. DFT and TD-DFT computations were performed to characterize the excited states. The computations showed that in the GS, the planar conformation is the most energetically favorable, but the energy barrier to achieve 90° conformation is only ca. 25 meV (~200 cm⁻¹) for D-C4-NAP (Fig. 7a); a similar barrier of ca. 170 cm⁻¹ was recently measured for torsional motion of butadiyne-linked porphyrin dimers.⁷² The low barrier results in a broad distribution of θ conformations in the GS. Excited state computations showed that the oscillator strength for both S_1 and S_2 states depends strongly on θ and that the two dependences are complementary: for small θ angles the GS→ S_1 transition is bright while the GS→ S_2 transition is dark; opposite is observed for large θ angles: the GS→ S_1 transition is dark while the GS→ S_2 transition is bright (Fig. 7b). As a result, the 400 nm pulses excite an S_1 state in compounds with small θ angles, producing a hot S_1 state with ca. 5000 cm⁻¹ excess of vibrational energy, and an S_2 state in compounds with large θ angles. Note that 400 nm excitation wavelength is at the tail of the S_1 absorption peak, centered at 460 nm (Fig. 2), so the S_2 state excitation at 400 nm is more efficient than the S_1 excitation. Normal modes were computed for the S_1 and S_2 states as a function of θ (Fig. 7c). In the highly polar S_1 state, the frequencies of both C≡C modes decrease with an increase of the dihedral angle: the $\nu_{CC,ss}$ changes by ca. 150 cm⁻¹ (Fig. 7c), in agreement with the experimental observations. Very high IR intensities, exceeding 20000 km/mol, were found for the $\nu_{CC,ss}$ in the S_1 state, shown in Fig. 7c with circles having diameters proportional to the IR intensity. The IR intensities of $\nu_{CC,as}$ in S_1 and of both $\nu_{CC,ss}$ and $\nu_{CC,as}$ in S_2 are about ten-fold smaller (Fig. 7c, Table S1).

The C≡C absorption spectrum in the excited states was modeled at zero time and at 10 ps following excitation using the computed C≡C frequencies in the S_1 and S_2 states and their IR intensities,

angular Boltzmann (θ) distribution of the ground-state conformations, and oscillator strengths of the S_2 and S_1 transitions. The relative population of the S_1 and S_2 states after 400 nm excitation was the only free parameter in the modelling (Fig. 7d, solid lines). The modelling predicts double-peak shapes for both early time and 10 ps spectra with the red-shifted peak growing with time. The overall peak shifts are larger than those observed in the experiment, but the overall similarity between of the observed and simulated transients is impressive. While simple analysis of the experimental transient C \equiv C spectra may suggest that the two observed peaks originate from different excited states, mostly S_2 for the high frequency peak and mostly S_1 for the low frequency peak, the modeling indicates that both peaks originate predominantly from the S_1 state, just from different θ conformations.

Modeling of the spectral dynamics in m-IR. The initial C \equiv C peak found at small delays predominantly at 2090 cm^{-1} is mostly due to directly excited S_1 states, thus representing compounds with small θ angles. The $\nu_{\text{CC,ss}}$ frequency in S_1 for $\theta = 0 - 30^\circ$ is centered at ca. 2160 cm^{-1} (Fig. 7c). The compounds featuring $\theta > 50^\circ$ are excited to the S_2 state; their relaxation occurs with a characteristic time of ca. 5.5 ps and results in formation of the S_1 states with the same θ angles. The red-shifted $\nu_{\text{CC,ss}}$ peak that appears at later time delays arises mostly from the $\nu_{\text{CC,ss}}$ mode in the S_1 state for $\theta > 50^\circ$; it is centered at ca. 2055 cm^{-1} (Fig. 7c). The calculations confirm that the observed C \equiv C peak alternation is caused by $S_2 \rightarrow S_1$ relaxation. There is a significant contribution to the blue C \equiv C peak from the $\nu_{\text{CC,as}}$ in the S_2 state with $\theta \sim 90^\circ$ (Fig. 7c, gray line and circles). $S_2 \rightarrow S_1$ relaxation for such conformations produces a slight decrease in the high-frequency C \equiv C peak amplitude, as observed in the experiment.

To evaluate the extent of charge separation in the S_1 state, the dipole moment of the compound in the S_1 state was computed for various θ angles (Fig. 7e). The dipole moment increases as θ approaches ca. 39 D, which corresponds to a separation distance of 8.1 Å for a full electron charge. Note that the bridge length is about 6.7 Å, indicating that the S_1 state for D-C4-NAP manifests complete charge separation. Figure 7e confirms that, for the CS state, the C \equiv C frequencies report the extent of charge separation: larger θ angles feature smaller $\nu_{\text{CC,ss}}$ frequencies and larger charge separation (Fig. S6). Note however, that such correlation is not observed for acceptor-localized excited states featuring a small charge separation extent, as apparent for the S_2 state where strongly varying C \equiv C mode frequencies correspond to essentially the same dipole moment of the molecule (Fig. 7c, Table S5).

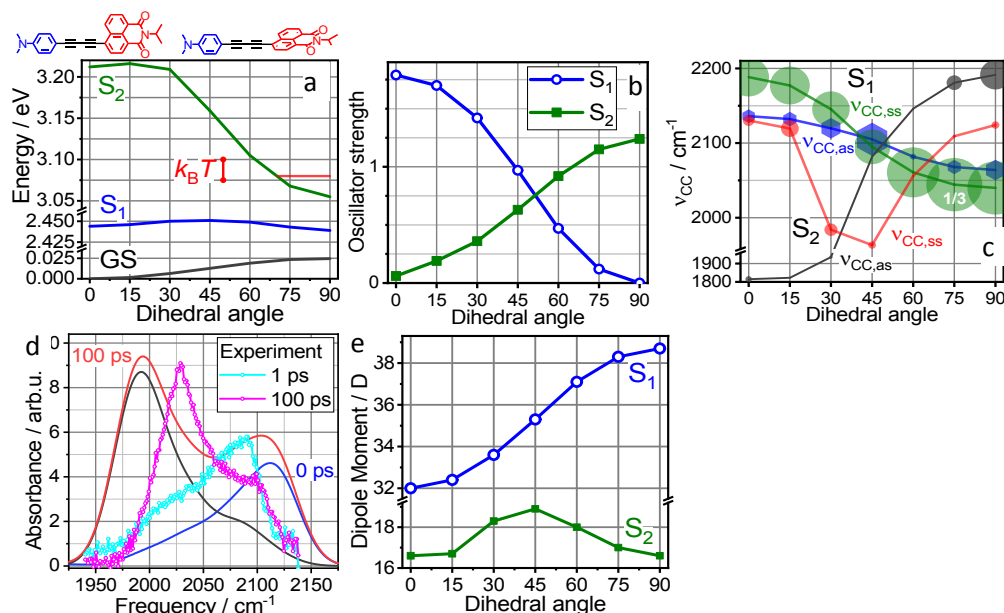


Fig. 7. Energies (a) of the ground state (GS) and S_1 and S_2 singlet excited states and the S_1 , S_2 oscillator strengths (b) as a function of the dihedral angle, θ , for D-C4-NAP in DCM. (c) Dihedral angle dependence of the $\nu_{CC,as}$ and $\nu_{CC,ss}$ frequencies for the S_1 (green and blue) and S_2 states (red and grey). The symbol sizes are proportional to the IR intensity of the mode (the IR intensities for the $\nu_{CC,ss}$ mode in the S_1 state were scaled by 1/3 factor not to overwhelm the graph). (d) Modeling of the absorption spectrum for the ν_{CC} modes at zero time (blue line) and at 100 ps (red line). The black line shows the contribution due to the $S_2 \rightarrow S_1$ relaxation. The experimental transient absorption spectra at indicated time delays are also shown. (e) Dipole moment of D-C4-NAP in DCM computed for the S_1 and S_2 states vs. the dihedral angle.

Symmetry origin of the $S_1 - S_2$ oscillator strength variations with θ . To explore the reasons that the S_1 and S_2 oscillator strength alternates as a function of θ , we performed natural transition orbitals analysis.⁷³ The natural orbitals for $S_0 \rightarrow S_1$ and $S_0 \rightarrow S_2$ transitions at $\theta = 0^\circ$ (left) and $\theta = 90^\circ$ (right) are shown in Figure 8. The symmetry of the natural orbitals with respect to the plane perpendicular to the acceptor plane passing through the C4 bridge is indicated for each orbital. For $\theta = 0^\circ$, the $S_0 \rightarrow S_1$ transition is symmetry allowed involving symmetric orbitals, whereas the $S_0 \rightarrow S_2$ transition is symmetry forbidden, involving antisymmetric \rightarrow symmetric and symmetric \rightarrow antisymmetric orbitals (Fig. 8) The principle is illustrated schematically in Scheme 3. At $\theta = 90^\circ$ the $S_0 \rightarrow S_1$ transition is forbidden (antisymmetric \rightarrow symmetric), while the $S_0 \rightarrow S_2$ transition is allowed (symmetric \rightarrow symmetric, Fig. 8). This analysis points to symmetry as the main reason behind the alternation of the oscillator strength in the S_1 and S_2 states (Fig. 7).

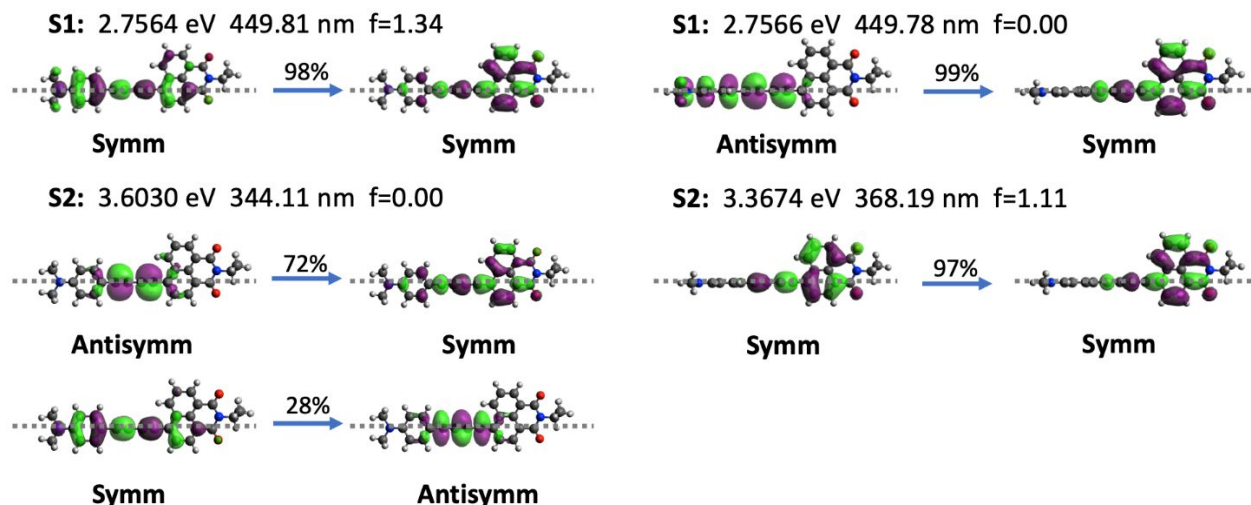
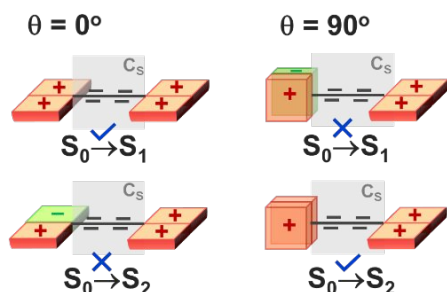


Fig. 8. Leading natural transition orbitals for $S_0 \rightarrow S_1$ and $S_0 \rightarrow S_2$ transitions of D-C4-NAP with their contributions in % above the arrow. The transition energy (in eV), transition wavelength, and the oscillator strength (f) values are shown. The symmetry of the orbitals with respect to the plane shown with dots is indicated. Note that the acceptor as a whole is not symmetric with respect to the plane; therefore, only the symmetry of the acceptor motif attached to the bridge is considered.



Scheme 3. Cartoon illustrating how symmetry affects the electronic coupling between the ground and S_1 , S_2 excited states.

Interestingly, the S_2 energy surface has a minimum at 90° , which is sufficiently deep ($\sim 8k_B T$) to alter significantly the torsion angle distribution that existed in the GS (Fig. 7a). If the S_2 lifetime is comparable or longer than the internal rotational time, dynamic population of DBA conformations with larger θ angle will occur. Such orthogonalization may change the relaxation rate to S_1 , depending on the angular dependence of the $S_2 - S_1$ coupling strength. The calculations, using the GMH approach,⁶⁷ revealed that the $S_2 - S_1$ coupling is the largest at $\theta \sim 30^\circ$ and decreases monotonically towards both 0° and 90° (Fig. 9). Therefore, the dynamic orthogonalization is capable of dramatically reducing k_{CS} for the D-C4-NAP compound. Under the conditions studied, however, the mean S_2 lifetime is shorter than the θ rotational time, preventing a clear observation of this effect.

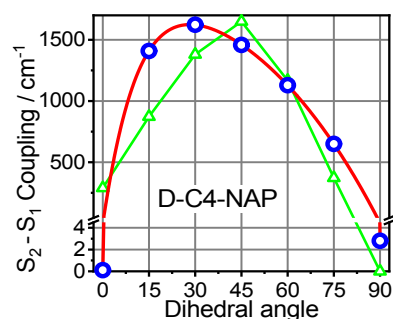


Fig. 9. The TD-DFT computed S_2 - S_1 coupling strength as a function of the dihedral angle, θ (blue circles and red line for eye guidance) for D-C4-NAP and the product of f_1 and f_2 , the oscillator strengths of the S_1 and S_2 states, respectively (green).

$S_2 - S_1$ electronic coupling varies with θ . The computed electronic $S_2 - S_1$ coupling is small at 0 and 90°, peaking at ca. 30° (Fig. 9). The dependence of the coupling strength on θ originates with the orbital overlap between the donor and acceptor fragments as a function of angle. The small coupling strength at 0 and 90° can be understood in the context of the symmetries associated with the $S_0 \rightarrow S_1$ and $S_0 \rightarrow S_2$ transitions. At both 0 and 90°, S_1 and S_2 states feature opposite symmetries (Fig. 7b), which result in near zero $S_2 - S_1$ couplings at these angles. The maximal coupling is realized at ca. 30°, where the symmetry is low and both transitions from the ground state are allowed. As a result, the S_2 - S_1 coupling θ -dependence tracks the product of the f_1 and f_2 oscillator strengths (Fig. 9c, green, normalized).

Large values of the coupling strength at $\theta = 15$ -60° suggest that the S_1 and S_2 states are mixed to a significant extent at these angles. A signature of this mixing is seen in the increase of the dipole moment of the S_2 state (Fig. 7e). Adiabatic ET likely takes place at angles in this range. The ET process at smaller coupling strength ($\theta < 10^\circ$ and $>75^\circ$) is likely nonadiabatic. The Marcus theory ET rate with $G^\circ = -0.5$ eV and $\lambda_{\text{total}} = 1$ eV, $(k_{\text{CS}})^{-1}$ was computed at 4.6 ps for a coupling strength of 100 cm^{-1} , which corresponds to the angle of ca. 88°. It is surprising to see that the experimentally measured CS rates correspond to such a narrow window of torsion angles ($>83^\circ$).

To test the extent the butadiyne bridge can bend we performed DFT energy calculations at different bend angles for two torsion angles, 0° and 60° (Fig. S10). We found that the range of bend angles thermally accessible at room temperature is rather narrow (165 – 180°). Moreover, the state energies and transition dipole moments are found to be weakly dependent on the bend angle (Fig. S10). The results suggest that the analysis performed with the linear bridge structures is robust with respect to the bend angle deviations.

Concluding remarks

In summary, we characterized the excited state dynamics for a set of novel DBA compounds featuring a butadiyne bridge using transient absorption spectroscopy in the visible and mid-IR regions and electronic structure calculations. While the bridge, in general, enables strong state coupling and conjugation, we found that it is the symmetry of the frontier orbitals that plays the major role in identifying

the coupling pattern among the electronic states. This symmetry is affected greatly by the dihedral angle. For the D-C4-NAP species, the symmetry dictates that the S_1 state is bright only for conformations with small dihedral angles, while the S_2 state is bright for conformations with large dihedral angles. This finding offers the opportunity to utilize photo-selection upon excitation, such that while both S_1 and S_2 states became excited at specific excitation wavelength, the dihedral angles in the S_1 and S_2 states are very different. For example, with 400 nm excitation of D-C4-NAP the S_1 state will possess small dihedral angles, while S_2 electronic excited states will possess large dihedral angles close to 90° . Note that this photoselection is different from an ability of selecting particular geometries by exciting at different frequencies. We have shown that the S_1 state in D-C4-NAP is predominantly the CSS, characterized by a θ -dependent dipole moment of 32 – 39 D, with the largest value at $\theta = 90^\circ$. Moreover, the frontier orbital symmetry affects greatly the coupling of the S_2 and S_1 states; the coupling at $\theta = 90^\circ$ was computed to be ca. 500-fold smaller than that at $\theta = 30^\circ$. The $S_2 \rightarrow S_1$ relaxation, which constitutes a CS reaction, occurs with different rates for different dihedral angles. An indication of the rate distribution was observed in variations of the CS rates obtained from fitting of kinetics at different observation wavelengths. The mean values for k_{CS} were measured at ca. 5.5 and 11.4 ps for D-C4-NAP in DCM and toluene, respectively. An additional component of 50 – 180 ps was observed from the global fit of the transient data. This time component is assigned to the rotational motion resulting in the changes of the dihedral angle, θ . Because of at least an order of magnitude difference between k_{CS} and k_{rot} , the influence of the rotation onto the CS process has not been observed clearly. The decay process of CSS (k_{CR} or k_{ISC}) is at least several fold slower than k_{rot} . Therefore, the rotational process may affect the recombination in a significant way, but the current measurements did not permit a clear separation of such processes. We found that the polarization of the charge separated state correlates with the frequency of the $C \equiv C$ stretching modes of the bridge, supported by the TD-DFT modeling.

Interestingly, the S_1 (CS) state for D-C4-NAP in DCM became lower in energy than the NAP-localized triplet state, preventing formation of the latter and resulting in a ca. 0.4 ns lifetime for the charge separated state. For the Ph-C4-NAP species, the diabatic CS state occurs at higher energies where a larger number of D- and A-localized diabatic states are found; stronger mixing of these states produces a much lower extent of polarization in the eigenstates. The D-C4-NAP compound offers exciting opportunities for ET-rate modulation by exciting vibrational modes on the bridge,^{53, 74-78} which will be reported in a separate manuscript.

Acknowledgements

We thank the National Science Foundation for generously supporting these studies (CHE-1565427 to IVR, CHE-1565812 to DNB, and CHE-1764347 to TR). SDB thanks Purdue University for a Cagiantas Fellowship. JV gratefully acknowledges support of a Fulbright-Garcia Robles Scholarship and a Graduate Program in Nanoscience (GP-Nano) Fellowship from Duke University. We also thank Mr. Adharsh Raghavan for assistance in acquiring C13 NMR spectra.

Supplementary Materials description: DFT-computed state energies, orbital compositions and normal mode frequencies for different electronic states at different torsion angles, transient IR data for Si-C4-NAP in toluene and synthesis details.

References

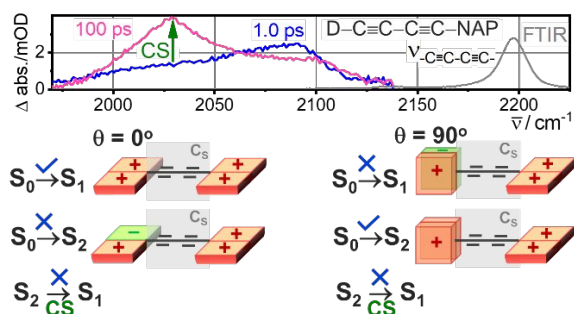
1. T. V. Duncan, P. P. Ghoroghchian, I. V. Rubtsov, D. A. Hammer and M. J. Therien, *J. Am. Chem. Soc.*, 2008, **130**, 9773-9784.
2. B. Shan, A. Nayak, O. F. Williams, D. C. Yost, N. F. Polizzi, Y. Liu, N. Zhou, Y. Kanai, A. M. Moran, M. J. Therien and T. J. Meyer, *Proc. Natl. Acad. Sci.*, 2019, **116**, 16198-16203.
3. Y. Shi, D. Frattarelli, N. Watanabe, A. Facchetti, E. Cariati, S. Righetto, E. Tordin, C. Zuccaccia, A. Macchioni, S. L. Wegener, C. L. Stern, M. A. Ratner and T. J. Marks, *J. Am. Chem. Soc.*, 2015, **137**, 12521-12538.
4. Y. S. Bai, J. Rawson, S. A. Roget, J. H. Olivier, J. X. Lin, P. Zhang, D. N. Beratan and M. J. Therien, *Chem. Sci.*, 2017, **8**, 5889-5901.
5. L. Fenenko, G. Shao, A. Orita, M. Yahiro, J. Otera, S. Svehnikov and C. Adachi, *Chem. Commun.*, 2007, DOI: 10.1039/B700466D, 2278-2280.
6. A. Nayak, J. Park, K. De Mey, X. Q. Hu, T. V. Duncan, D. N. Beratan, K. Clays and M. J. Therien, *ACS Central Sci.*, 2016, **2**, 954-966.
7. Y. K. Kang, P. Zhang, I. V. Rubtsov, J. R. Zheng, G. Bullard, D. N. Beratan and M. J. Therien, *J. Phys. Chem. B*, 2019, **123**, 10456-10462.
8. N. F. Polizzi, T. Jiang, D. N. Beratan and M. J. Therien, *Proc. Natl. Acad. Sci.*, 2019, **116**, 14465-14470.
9. F. Dumur, N. Gautier, N. Gallego-Planas, Y. Şahin, E. Levillain, N. Mercier, P. Hudhomme, M. Masino, A. Girlando, V. Lloveras, J. Vidal-Gancedo, J. Veciana and C. Rovira, *J. Org. Chem.*, 2004, **69**, 2164-2177.
10. H. M. Heitzer, T. J. Marks and M. A. Ratner, *J. Am. Chem. Soc.*, 2015, **137**, 7189-7196.
11. J. Kandhadi, V. Yeduru, P. R. Bangal and L. Giribabu, *Phys. Chem. Chem. Phys.*, 2015, **17**, 26607-26620.
12. M.-B. S. Kirketerp, M. Å. Petersen, M. Wanko, H. Zettergren, A. Rubio, M. B. Nielsen and S. B. Nielsen, *ChemPhysChem*, 2010, **11**, 2495-2498.
13. C. Van Dyck and M. A. Ratner, *Nano Lett.*, 2015, **15**, 1577-1584.
14. Y. Yamazaki, A. Umemoto and O. Ishitani, *Inorg. Chem.*, 2016, **55**, 11110-11124.
15. N. M. Dickson-Karn, C. M. Olson, W. C. W. Leu and C. S. Hartley, *J. Phys. Org. Chem.*, 2014, **27**, 661-669.
16. D. P. Hoffman, O. P. Lee, J. E. Millstone, M. S. Chen, T. A. Su, M. Creelman, J. M. J. Fréchet and R. A. Mathies, *J. Phys. Chem. C*, 2013, **117**, 6990-6997.
17. A. B. Ricks, K. E. Brown, M. Wenninger, S. D. Karlen, Y. A. Berlin, D. T. Co and M. R. Wasielewski, *J. Am. Chem. Soc.*, 2012, **134**, 4581-4588.
18. A. B. Ricks, G. C. Solomon, M. T. Colvin, A. M. Scott, K. Chen, M. A. Ratner and M. R. Wasielewski, *J. Am. Chem. Soc.*, 2010, **132**, 15427-15434.
19. M. Kivala and F. Diederich, *Acc. Chem. Res.*, 2009, **42**, 235-248.
20. S. Priyadarshy, M. J. Therien and D. N. Beratan, *J. Am. Chem. Soc.*, 1996, **118**, 1504-1510.
21. F. J. Rizzuto, C. Hua, B. Chan, T. B. Faust, A. Rawal, C. F. Leong, J. M. Hook, C. J. Kepert and D. M. D'Alessandro, *Phys. Chem. Chem. Phys.*, 2015, **17**, 11252-11259.
22. C. Van Dyck, T. J. Marks and M. A. Ratner, *ACS Nano*, 2017, **11**, 5970-5981.

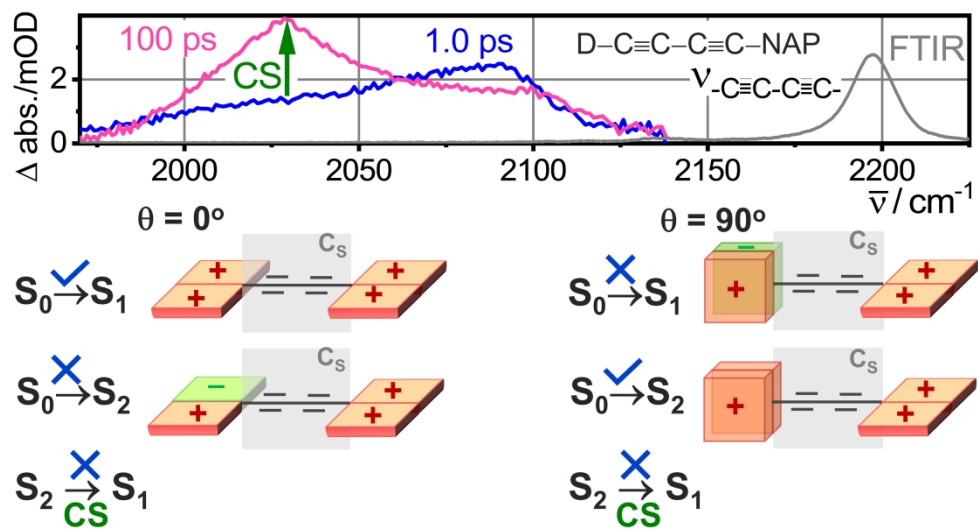
23. R. B. Wang, A. M. Brugh, J. Rawson, M. J. Therien and M. D. E. Forbes, *J. Am. Chem. Soc.*, 2017, **139**, 9759-9762.
24. M. E. Smith, E. L. Flynn, M. A. Fox, A. Trottier, E. Wrede, D. S. Yufit, J. A. K. Howard, K. L. Ronayne, M. Towrie, A. W. Parker, F. Hartl and P. J. Low, *Chem. Commun.*, 2008, DOI: 10.1039/B811357B, 5845-5847.
25. M. Hoffmann, J. Karnbratt, M. H. Chang, L. M. Herz, B. Albinsson and H. L. Anderson, *Angew. Chem.-Int. Edit.*, 2008, **47**, 4993-4996.
26. W. C. W. Leu, A. E. Fritz, K. M. Digianantonio and C. S. Hartley, *J. Org. Chem.*, 2012, **77**, 2285-2298.
27. W. C. W. Leu and C. S. Hartley, *Org. Lett.*, 2013, **15**, 3762-3765.
28. D. Nilsson, S. Watcharinyanon, M. Eng, L. Li, E. Moons, L. S. O. Johansson, M. Zharnikov, A. Shaporenko, B. Albinsson and J. Mårtensson, *Langmuir*, 2007, **23**, 6170-6181.
29. A. Heckmann and C. Lambert, *Angew. Chem. Int. Ed.*, 2012, **51**, 326-392.
30. M. I. Bruce, *Chem. Rev.*, 1998, **98**, 2797-2858.
31. E. Göransson, R. Emanuelsson, K. Jorner, T. F. Markle, L. Hammarström and H. Ottosson, *Chem. Sci.*, 2013, **4**, 3522-3532.
32. M. U. Winters, J. Kärnbratt, M. Eng, C. J. Wilson, H. L. Anderson and B. Albinsson, *J. Phys. Chem. C*, 2007, **111**, 7192-7199.
33. A. K. Pati, S. J. Gharpure and A. K. Mishra, *J. Phys. Chem. A*, 2016, **120**, 5838-5847.
34. A. K. Pati, M. Mohapatra, P. Ghosh, S. J. Gharpure and A. K. Mishra, *J. Phys. Chem. A*, 2013, **117**, 6548-6560.
35. A. K. Pati, S. J. Gharpure and A. K. Mishra, *Phys. Chem. Chem. Phys.*, 2014, **16**, 14015-14028.
36. C. E. Tait, P. Neuhaus, M. D. Peeks, H. L. Anderson and C. R. Timmel, *Phys. Chem. Chem. Phys.*, 2016, **18**, 5275-5280.
37. M. U. Winters, J. Karnbratt, H. E. Blades, C. J. Wilson, M. J. Frampton, H. L. Anderson and B. Albinsson, *Chem.-Eur. J.*, 2007, **13**, 7385-7394.
38. B. Albinsson, M. P. Eng, K. Pettersson and M. U. Winters, *Phys. Chem. Chem. Phys.*, 2007, **9**, 5847-5864.
39. J. Daub, R. Engl, J. Kurzawa, S. E. Miller, S. Schneider, A. Stockmann and M. R. Wasielewski, *J. Phys. Chem. A*, 2001, **105**, 5655-5665.
40. W. B. Davis, M. A. Ratner and M. R. Wasielewski, *J. Am. Chem. Soc.*, 2001, **123**, 7877-7886.
41. O. S. Wenger, *Chem. Soc. Rev.*, 2011, **40**, 3538-3550.
42. J. Valdiviezo and J. L. Palma, *J. Phys. Chem. C*, 2018, **122**, 2053-2063.
43. I. V. Rubtsov, N. P. Redmore, R. M. Hochstrasser and M. J. Therien, *J. Am. Chem. Soc.*, 2004, **126**, 2684-2685.
44. A. C. Benniston, A. Harriman, P. Li, P. V. Patel and C. A. Sams, *Phys. Chem. Chem. Phys.*, 2005, **7**, 3677-3679.
45. R. A. Marcus and N. Sutin, *Biochim. Biophys. Acta*, 1985, **811**, 265-322.
46. D. N. Beratan, S. S. Skourtis, I. A. Balabin, A. Balaeff, S. Keinan, R. Venkatramani and D. Xiao, *Acc. Chem. Res.*, 2009, **42**, 1669-1678.
47. D. N. Beratan, C. Liu, A. Migliore, N. F. Polizzi, S. S. Skourtis, P. Zhang and Y. Zhang, *Acc. Chem. Res.*, 2015, **48**, 474-481.
48. S. S. Skourtis, D. H. Waldeck and D. N. Beratan, *Ann. Rev. Phys. Chem.*, 2010, **61**, 461-485.
49. M. P. Eng and B. Albinsson, *Chem. Phys.*, 2009, **357**, 132-139.
50. J. Blumberger, *Chem. Rev.*, 2015, **115**, 11191-11238.
51. H. Oberhofer, K. Reuter and J. Blumberger, *Chem. Rev.*, 2017, **117**, 10319-10357.

52. F. Jiang, D. I. Trupp, N. Algethami, H. Zheng, W. He, A. Alqorashi, C. Zhu, C. Tang, R. Li, J. Liu, H. Sadeghi, J. Shi, R. Davidson, M. Korb, A. N. Sobolev, M. Naher, S. Sangtarash, P. J. Low, W. Hong and C. J. Lambert, *Angew. Chem. Int. Ed.*, 2019, **58**, 18987-18993.
53. Z. Lin, C. M. Lawrence, D. Xiao, V. V. Kireev, S. S. Skourtis, J. L. Sessler, D. N. Beratan and I. V. Rubtsov, *J. Am. Chem. Soc.*, 2009, **131**, 18060-18062.
54. Y. Yue, T. Grusenmeyer, Z. Ma, P. Zhang, R. H. Schmehl, D. N. Beratan and I. V. Rubtsov, *Dalton Trans.*, 2015, **44**, 8609-8616.
55. Z. Ma, Z. Lin, C. M. Lawrence, I. V. Rubtsov, P. Antoniou, S. S. Skourtis, P. Zhang and D. N. Beratan, *Chem. Sci.*, 2018, **9**, 6395-6405.
56. I. V. Rubtsov, Y. K. Kang, N. P. Redmore, R. M. Allen, J. R. Zheng, D. N. Beratan and M. J. Therien, *J. Am. Chem. Soc.*, 2004, **126**, 5022-5023.
57. M. D. Fayer, *Elements of quantum mechanics*, Oxford University Press, 2001.
58. P. Siemsen, R. C. Livingston and F. Diederich, *Angew. Chem. Int. Ed.*, 2000, **39**, 2633-2657.
59. Y. Yue, T. Grusenmeyer, Z. Ma, P. Zhang, R. H. Schmehl, D. N. Beratan and I. V. Rubtsov, *J. Phys. Chem. A*, 2014, **118**, 10407-10415.
60. Y. K. Yue, T. Grusenmeyer, Z. Ma, P. Zhang, T. T. Pham, J. T. Mague, J. P. Donahue, R. H. Schmehl, D. N. Beratan and I. V. Rubtsov, *J. Phys. Chem. B*, 2013, **117**, 15903-15916.
61. H. S. Yu, X. He, S. L. Li and D. G. Truhlar, *Chem. Sci.*, 2016, **7**, 5032-5051.
62. F. Weigend and R. Ahlrichs, *Phys. Chem. Chem. Phys.*, 2005, **7**, 3297-3305.
63. M. J. Frisch, G. W. Trucks, H. B. Schlegel, G. E. Scuseria, M. A. Robb, J. R. Cheeseman, G. Scalmani, V. Barone, G. A. Petersson, H. Nakatsuji, X. Li, M. Caricato, A. V. Marenich, J. Bloino, B. G. Janesko, R. Gomperts, B. Mennucci, H. P. Hratchian, J. V. Ortiz, A. F. Izmaylov, J. L. Sonnenberg, Williams, F. Ding, F. Lipparini, F. Egidi, J. Goings, B. Peng, A. Petrone, T. Henderson, D. Ranasinghe, V. G. Zakrzewski, J. Gao, N. Rega, G. Zheng, W. Liang, M. Hada, M. Ehara, K. Toyota, R. Fukuda, J. Hasegawa, M. Ishida, T. Nakajima, Y. Honda, O. Kitao, H. Nakai, T. Vreven, K. Throssell, J. A. Montgomery Jr., J. E. Peralta, F. Ogliaro, M. J. Bearpark, J. J. Heyd, E. N. Brothers, K. N. Kudin, V. N. Staroverov, T. A. Keith, R. Kobayashi, J. Normand, K. Raghavachari, A. P. Rendell, J. C. Burant, S. S. Iyengar, J. Tomasi, M. Cossi, J. M. Millam, M. Klene, C. Adamo, R. Cammi, J. W. Ochterski, R. L. Martin, K. Morokuma, O. Farkas, J. B. Foresman and D. J. Fox, *Journal*, 2016.
64. T. Yanai, D. P. Tew and N. C. Handy, *Chem. Phys. Lett.*, 2004, **393**, 51-57.
65. G. Scalmani and M. J. Frisch, *J. Chem. Phys.*, 2010, **132**, 114110.
66. A. G. Baboul and H. B. Schlegel, *J. Chem. Phys.*, 1997, **107**, 9413-9417.
67. R. J. Cave and M. D. Newton, *Chem. Phys. Lett.*, 1996, **249**, 15-19.
68. K. Aidas, C. Angeli, K. L. Bak, V. Bakken, R. Bast, L. Boman, O. Christiansen, R. Cimiraglia, S. Coriani, P. Dahle, E. K. Dalskov, U. Ekström, T. Enevoldsen, J. J. Eriksen, P. Ettenhuber, B. Fernández, L. Ferrighi, H. Fliegl, L. Frediani, K. Hald, A. Halkier, C. Hättig, H. Heiberg, T. Helgaker, A. C. Hennum, H. Hetttema, E. Hjertenæs, S. Høst, I.-M. Høyvik, M. F. Iozzi, B. Jansík, H. J. A. Jensen, D. Jonsson, P. Jørgensen, J. Kauczor, S. Kirpekar, T. Kjærgaard, W. Klopper, S. Knecht, R. Kobayashi, H. Koch, J. Kongsted, A. Krapp, K. Kristensen, A. Ligabue, O. B. Lutnæs, J. I. Melo, K. V. Mikkelsen, R. H. Myhre, C. Neiss, C. B. Nielsen, P. Norman, J. Olsen, J. M. H. Olsen, A. Osted, M. J. Packer, F. Pawłowski, T. B. Pedersen, P. F. Provasi, S. Reine, Z. Rinkevicius, T. A. Ruden, K. Ruud, V. V. Rybkin, P. Sałek, C. C. M. Samson, A. S. de Merás, T. Saue, S. P. A. Sauer, B. Schimmelpfennig, K. Sneskov, A. H. Steindal, K. O. Sylvester-Hvid, P. R. Taylor, A. M. Teale, E. I. Tellgren, D. P. Tew, A. J. Thorvaldsen, L. Thøgersen, O. Vahtras, M. A. Watson, D. J. D. Wilson, M. Ziolkowski and H. Ågren, *WIREs Computational Molecular Science*, 2014, **4**, 269-284.
69. M.-L. Horng, J. A. Gardecki and M. Maroncelli, *J. Phys. Chem. A*, 1997, **101**, 1030-1047.
70. P. Hamm, S. M. Ohline and W. Zinth, *J. Chem. Phys.*, 1997, **106**, 519-529.

71. N. I. Rubtsova and I. V. Rubtsov, *Ann. Rev. Phys. Chem.*, 2015, **66**, 717-738.
72. M. D. Peeks, P. Neuhaus and H. L. Anderson, *Phys. Chem. Chem. Phys.*, 2016, **18**, 5264-5274.
73. R. L. Martin, *J. Chem. Phys.*, 2003, **118**, 4775-4777.
74. D. Q. Xiao, S. S. Skourtis, I. V. Rubtsov and D. N. Beratan, *Nano Lett.*, 2009, **9**, 1818-1823.
75. Z. Ma, Z. Lin, Candace M. Lawrence, I. V. Rubtsov, P. Antoniou, S. S. Skourtis, P. Zhang and D. N. Beratan, *Chem. Sci.*, 2018, **9**, 6395-6405.
76. Y. K. Yue, T. Grusenmeyer, Z. Ma, P. Zhang, R. H. Schmehl, D. N. Beratan and I. V. Rubtsov, *Dalton Trans.*, 2015, **44**, 8609-8616.
77. M. Delor, S. A. Archer, T. Keane, A. Meijer, I. V. Sazanovich, G. M. Greetham, M. Towrie and J. A. Weinstein, *Nat. Chem.*, 2017, **9**, 1099-1104.
78. M. Delor, P. A. Scattergood, I. V. Sazanovich, A. W. Parker, G. M. Greetham, A. Meijer, M. Towrie and J. A. Weinstein, *Science*, 2014, **346**, 1492-1495.

TOC image:





TOC graphics

338x190mm (300 x 300 DPI)